ACS Photonics

Article

Cite This: ACS Photonics 2019, 6, 1493−1499

pubs.acs.org/journal/apchd5

Imaging Performance of Polarization-Insensitive Metalenses

Manuel Decker,*[,†] Wei Ting Chen,[‡] Thomas Nobis,[†] Alexander Y. Zhu,[‡] Mohammadreza Khorasaninejad,[‡] Zameer Bharwani,[‡,§] Federico Capasso,[‡] and Jörg Petschulat[∥]

[†]Corporate Research and Technology, Carl Zeiss AG, Carl-Zeiss-Promenade 10, 07745 Jena, Germany

[‡]Harvard John A. Paulson School of Engineering and Applied Sciences, Harvard University, Cambridge, Massachusetts 02138, United States

[§]University of Waterloo, Waterloo, Ontario, Canada

[∥]ZEISS Semiconductor Mask Solutions, Carl Zeiss SMT GmbH, Carl-Zeiss-Promenade 10, 07745 Jena, Germany

ABSTRACT: Metasurfaces have recently emerged as a promising technology to realize flat optical components with customized functionalities. In particular, their application to lenses in various imaging systems is of significant interest. However, a systematic and complete study of the focusing and imaging behavior of metalenses has not yet been conducted. In this work we analyze not only the on-axis focusing performance, but also the field-dependent wavefront aberrations via a phase-retrieval optimization method. We find that, particularly for high-NA metalenses, the field-dependent geometrical aberrations like coma are dominant at the design wavelength, while for longer and shorter operation wavelengths, the effective numerical aperture is decreased and mainly spherical aberrations are dominant. Additionally, we investigate the spectral and angular bandwidth of a polarization-insensitive metalens by analyzing the metalens efficiencies as a function of numerical aperture, field angle, and wavelength. We then compare the metalens performance to its refractive and diffractive counterparts and show how the respective metalens properties affect the imaging performance. For this purpose, we perform an imaging simulation for these three cases based on their field- and wavelength-dependent absolute deflection efficiencies and analyze the imaging properties of an extended test object. Our calculations show that metalenses can outperform diffractive lenses in terms of their angle-dependent efficiency for large deflection angles.

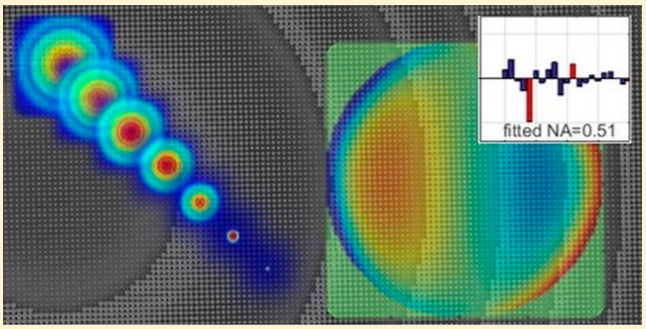

KEYWORDS: *metalens, polarization-independent, imaging, bandwidth, aberrations, field-dependency*

Metasurfaces offer an immense potential to freely engineer the dispersion, polarization properties as well as the wavefront of an incident beam with subwavelength resolution.[1−3] For this reason, research in metasurface devices, particularly metalenses,[4−8] has peaked in recent years. Metalenses are flat nanostructured surfaces that imprint a hyperbolic phase delay on the impinging wavefront for diffraction-limited focusing. This can be achieved by tailoring the design of the nanostructures at every position on the surface and their spatial distribution.[9] In contrast to conventional optical components that control light using gradual phase accumulation through propagation in bulk refractive materials, metalenses, as well as binary-blazed gratings,[4,10] rely on the optical properties of their nanoscale building blocks and their arrangement to generate the required spatial phase distribution. As such, they can provide extremely flat and lightweight implementations of lenses down to several hundred nanometers in thickness. The main concepts that are commonly used to generate a desired spatial phase delay include engineering waveguide properties (binary-blazed grating approach),[4,5,10] exploiting the geometrical phase (Pancharatnam-Berry phase),[6,7] and utilizing the local phase shifts of resonant nanoantennas, particularly in the Huygens' metasurface approach.[11−15] Typically, all-dielectric nanostructures composed of TiO_2, GaN, Si_3N_4, or Si, for example, are used as fundamental building blocks in order to avoid the losses inherent to metallic nanostructures and thus maximize the final efficiency of the device.[14−17] In this context, dielectric metalenses with a numerical aperture (NA) up to 1.4 and diffraction limited performance with a Strehl ratio of up to 0.8 for normal incidence have been reported.[18−22] Recently, several approaches to realize multiwavelength and even achromatic metalenses have also been successfully demonstrated.[23−29]

Nevertheless, when judging lens performance in general, the on-axis resolving power that is connected to the numerical aperture and the Strehl ratio is only one relevant aspect. In order to obtain a complete picture of lens performance one also needs to include the analysis of wavefront aberrations, dispersion properties and lens efficiency. All these aspects will ultimately manifest in the imaging behavior/quality of the lens

Received: February 8, 2019
Published: May 7, 2019

DOI: 10.1021/acsphotonics.9b00221
ACS Photonics 2019, 6, 1493−1499

and may result in (longitudinal and transversal) color errors, image distortions, vignetting, variations in image blur and contrast. Importantly, all these aberrations vary strongly depending on the angle of incidence or field angle when imaging extended objects. Consequently, when assessing the performance of metalenses, one needs to address all relevant aspects, in particular, the angular bandwidth as well as the lens efficiency. While a limited spectral bandwidth might not be relevant for specific imaging applications, the angular bandwidth of the lens, however, ultimately limits the numerical aperture as well as the etendue of the whole imaging system, that is, how much light can be funneled through the optical system under oblique incidence. A large angular bandwidth ensures uniform intensity of images and is of high practical importance. Furthermore, particularly for metalenses and sawtooth Fresnel lenses, due to the occurrence of diffraction, the overall focusing efficiencies and, vice versa, the amount of light that ends up in unwanted diffraction orders must be accounted for, as it can significantly deteriorate image quality.

In this paper, we analyze a NA = 0.8 polarization-independent metalens (PIM)[22] with respect to its on- and off-axis wavefront aberrations at three representative wavelengths (405, 532, and 660 nm). We exemplarily select a PIM based on the waveguide approach since polarization-insensitive optics is more widely applicable to practical applications (and not limited to circular polarization states, like the geometric phase approach) and since the higher angular bandwidth of the waveguide approach is more beneficial for imaging purposes. As such, our choice of the metalens represents the most suitable candidate for a benchmark comparison. For the latter purpose, we numerically analyze the spectral and angular bandwidths of the PIM in terms of efficiencies at several lens coordinates to simulate their overall imaging performance. We compare our findings to traditional refractive lenses as well as sawtooth Fresnel lenses and evaluate the metalens performance.

RESULTS AND DISCUSSION

Here, we exemplarily investigate a polarization-insensitive metalens consisting of TiO_2 nanopillars on a glass substrate. The nanopillars have a fixed height of H = 600 nm and their diameters are spatially varied from 100 to 220 nm in eight discrete steps to impart a specific hyperbolic phase profile given by $\phi(r) = -\frac{2\pi}{\lambda_d}(\sqrt{r^2 + f^2} - f)$ calculated via FDTD simulations. Here, λ_d = 532 nm is the design wavelength, f = 0.725 mm is the focal length, and r is the radial position on the PIM. The center-to-center distance between nanopillars is 250 nm to satisfy Nyquist sampling criteria. Qualitatively, the optical properties of nanopillars can be understood by treating nanopillars as a truncated waveguide. The transmitted light accumulates a phase delay mainly from the effective index n_{eff} of the fundamental HE11 mode[30] given by $\varphi = \frac{2\pi}{\lambda} n_{eff} H$. The larger the nanopillar diameter, the larger the n_{eff} and the phase delay.[19] We investigate a PIM with a nominal numerical aperture of NA = 0.8 and a lens diameter of 2 mm optimized for an operation wavelength of λ = 532 nm. Figure 1a and b show scanning-electron microscope (SEM) images and a photo of the PIM,[22] respectively.

In order to access the field-dependent wavefront aberrations of the PIM, we mount the metalens and the detection path on a single rail that can be rotated (see Figure 1c) and measure

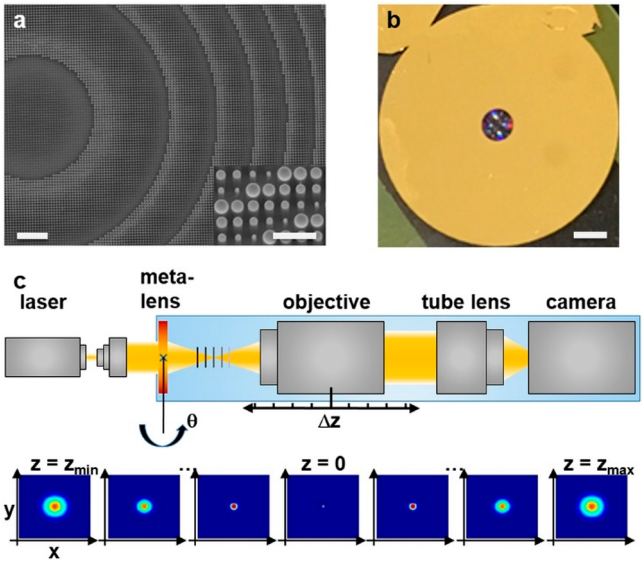

Figure 1. Images of the polarization-independent metalens (PIM) and a schematic diagram of the measurement setup. (a) Scanning electron microscope images and (b) photograph of the PIM. The center part is the PIM, while the surrounding yellow part is a gold thin film to block background light. The scale bars in (a) are 5 μm and 1 μm in the overview and inset images, respectively. The scale bar in (b) is 2 mm. (c) Scheme of the measurement setup for recording an oblique-incidence defocus stack as shown in the lower row. The wavefront aberration functions are deduced from the intensity profiles of these focal spots at different z-planes.

the wavefront properties for several angles of incidence (aoi) θ. Note that the PIM is positioned in the rotational center of the rail. The PIM is illuminated by collimated beams from various diode lasers with <1 nm line width. The light emerging from the PIM is collected by an objective lens (Olympus, NA = 0.95, 100×), followed by a tube lens with 180 mm focal length, and subsequently imaged onto a camera (IDS Inc. UI-1490SE). For each configuration (wavelength, angle of incidence) we recorded a defocus stack, that is, we took a series of images at different z-planes of the focal spot by changing the z-position of the objective (see Figure 1c). For the spacing of the z-slices in the defocus stack, we chose a range of ±3 Rayleigh lengths and discretized the range into 21 slices with a z-separation of 250 nm. One Rayleigh length is defined as 1RL = λ/NA^2 for λ = 532 nm and NA = 0.8.

From the experimental defocus stack, we retrieved the experimental phase profile and calculated the respective wavefront aberrations utilizing an iterative phase retrieval algorithm following the approach of ref 31. In our optimization procedure we propagate the complex pupil field $P(x_P,y_P) = A(x_P,y_P) \times \exp[ik \times W(x_P,y_P)]$ to the image plane. *The amplitude* $A(x_P,y_P)$ corresponds to the pupil amplitude function and $W(x_P,y_P)$ represents the wavefront aberrations. The resulting intensity stack is then optimized with respect to the measured input defocus stack using a Levenberg–Marquardt damped-least-squares optimization. The free parameters of the algorithm are the pupil function, the numerical aperture of the system, and the point-source size. Note that the fitted point-source size turned out to be diffraction-limited for all cases. The resulting pupil function is then decomposed into the orthogonal basis of Zernike polynomials Z_{mn} in polar coordinates using Fringe notation

DOI: 10.1021/acsphotonics.9b00221
ACS Photonics 2019, 6, 1493−1499

$W(r,\phi) = \sum_n \sum_{m=-n}^{n} c_{mn} Z_{mn}(r,\phi)$[32] and plotted in Figures 2, 3, and 4.

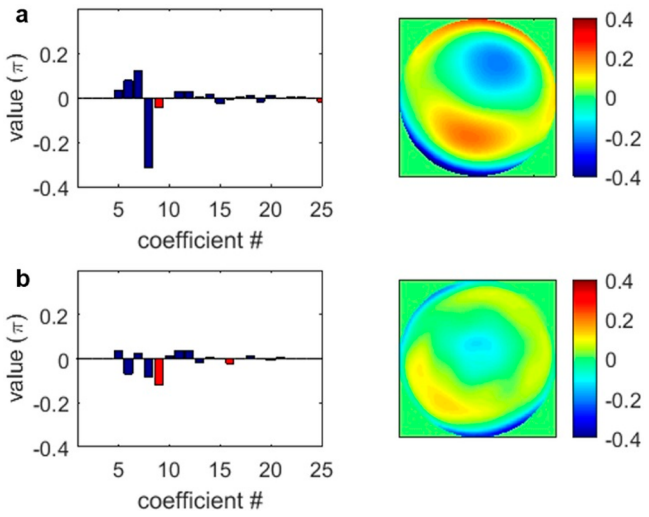

Figure 2. Experimental wavefront (phase) aberration plots in normalized units (right-hand side panel) and Zernike decompositions in Fringe notation (left-hand side panel, Z1-Z25) for (a) a NA = 0.8 reference objective and (b) the metalens. Both the metalens and the objective lens have the same NA of 0.8. This measurement was conducted at λ = 532 nm and at normal incidence. The objective has an entrance aperture that is about 2 mm larger than the entrance aperture of the metalens. The spherical-aberration contributions (Z4, Z9, Z16, Z25) are plotted in red for clarity. These results are extracted from experimental defocus stacks.

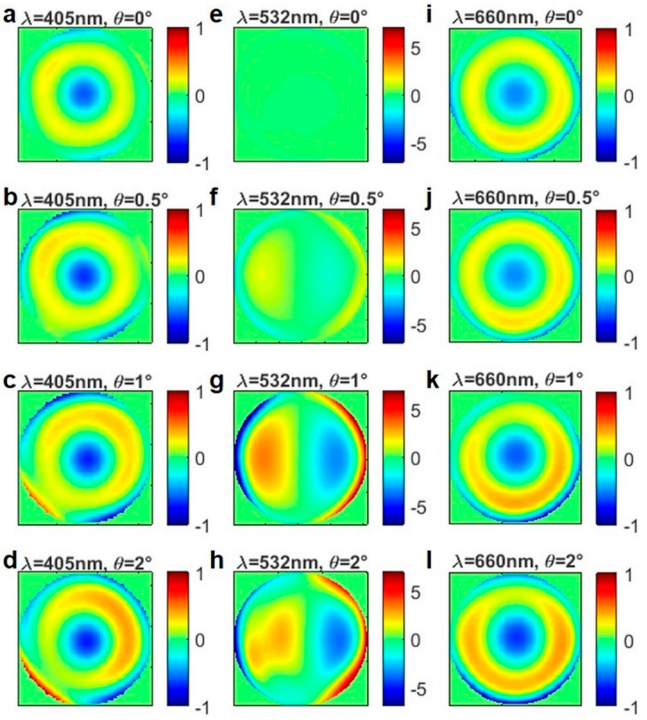

Figure 3. Measured wavefront (phase) aberration plots for the polarization-insensitive metalens at 405 (a–d), 532 (e–h), and 660 nm (i–l) wavelength as well as for angles of incidence $\theta_i = 0°$ (a, e, i), $\theta_i = 0.5°$ (b, f, j), $\theta_i = 1°$ (c, g, k), and $\theta_i = 2°$ (d, h, l). Note, the color scale in the second column (e–h) is seven times larger than that in the first and the third column to appropriately visualize the aberrations at the design wavelength.

To verify the PIM performance and get a complete picture of the on-axis wavefront aberrations, we measure a defocus stack of the metalens and a reference objective lens (Nikon, NA = 0.8, 100×) at 532 nm wavelength at normal incidence and compare the results in Figure 2. The left column shows the values for the corresponding Zernike coefficients (following Fringe notation, normalized with respect to π) for the reference objective (Figure 2a) and the PIM (Figure 2b), respectively. The corresponding wavefront (phase) aberrations (also normalized with respect to π) are plotted on the right column. Note that the first four Zernike coefficients (offset, x/y tilt, and defocus) are set to zero since they can be corrected via alignment and, therefore, are not relevant for the performance.

Figure 2 reveals that, indeed, at λ = 532 nm, on-axis performance in terms of wavefront aberrations of the PIM is better than for the reference objective, which suffers from coma (Z8) causing a reduction of the objective's Strehl ratio to around 0.4. The Strehl ratio is obtained from the RMS wavefront aberrations via the Marechal approximation.[33] For the PIM, in contrast, we obtain a Strehl ratio of 0.79 with the spherical aberration (Z9) being dominant. Thus, the PIM shows near diffraction-limited performance in this scenario. The fitted numerical aperture NA = 0.81 is close to the design NA of 0.8, so no stopping down of the lenses is observed. Our results are consistent with previous publications.[7,22]

In the second step, we now investigate the wavefront aberrations of the PIM at three different representative wavelengths λ = 405, 532, and 660 nm together with four different angles of incidence θ_i = 0°, 0.5°, 1°, and 2°. The retrieved wavefront aberration plots are shown in Figure 3 and the respective Zernike representation is shown in Figure 4.

From Figures 3 and 4 we learn that, for PIM operating at the design wavelength λ = 532 nm (middle column), it is mainly the coma aberrations that significantly increase with increasing field angle θ. This effect is inherent to (flat) single lenses due to the violation of the Abbe sine condition, especially for high numerical aperture lenses and can be corrected by constructing a lens doublet.[33−35] Importantly, the retrieved numerical aperture for all cases (Figures 3 and 4e–h) is around the nominal value of NA = 0.8.

The slightly larger values for the retrieved numerical aperture in Figure 4f–h result from the high spatial frequency components of the measured point-spread functions with severe coma (Z7 > 2) that are challenging for the optimization algorithm and can lead to numerical fluctuations that result in an artificially increased retrieved NA.

In contrast to operation at the design wavelength, for 405 and 660 nm wavelengths, the effective numerical aperture is significantly reduced to a value of around 0.5. The stopping down of the PIM's NA can be understood from the chromatic change of phase delay of the PIM as well as a dropping diffraction efficiency for oblique incidence, both leading to a reduction of the Strehl ratio. Furthermore, due to the latter effects, the coma aberration which was observed to be dominant at λ = 532 nm wavelength is qualitatively absent in this range of field angles (θ > 0°) and the spherical aberration becomes dominant. As a result, the PIM can still perform with reasonable spatial resolution (but a reduced NA) under monochromatic illumination even away from its design wavelength.

DOI: 10.1021/acsphotonics.9b00221
ACS Photonics 2019, 6, 1493−1499

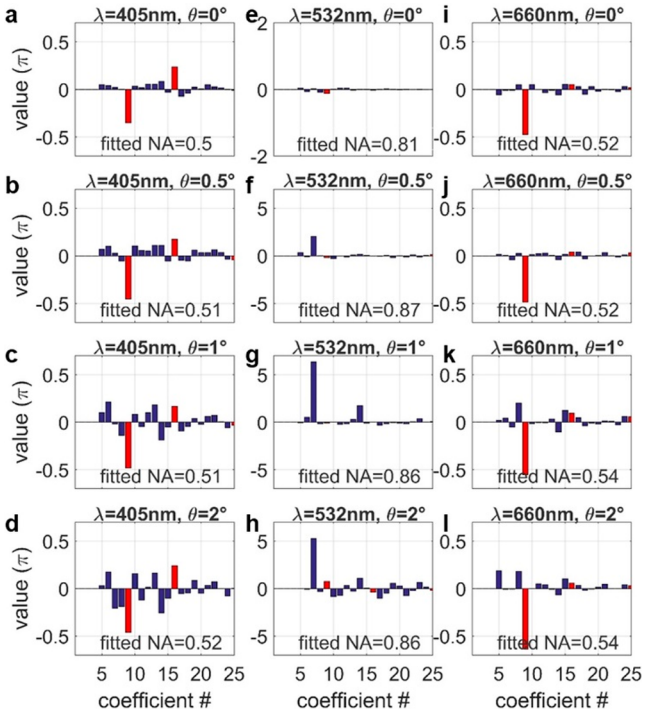

Figure 4. Zernike decomposition of the experimental wavefront aberration plots in Figure 3 (different wavelengths in the columns, different aoi in the rows). As in Figure 2, the (higher-order) spherical aberrations are plotted in red. Furthermore, the corresponding effective numerical apertures that were retrieved from our algorithm are given in each plot. Remarkably, a stopping down of the metalens numerical aperture to a value of approximately 0.5 is observed when the PIM is not operated at its design wavelength of 532 nm.

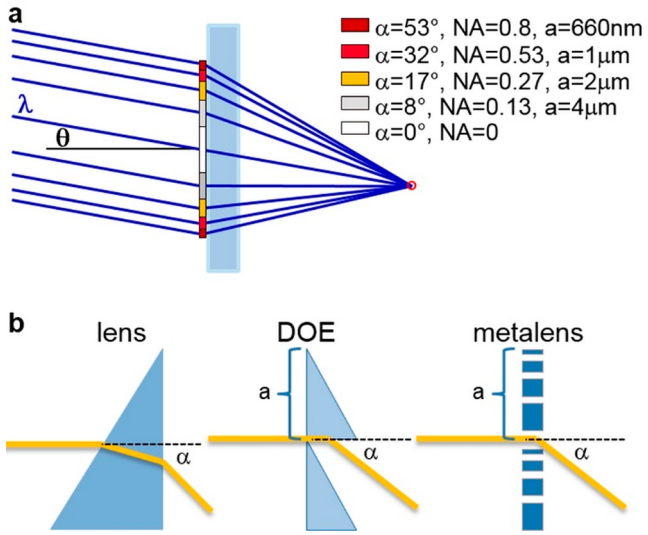

Figure 5. (a) Scheme of the simulation setup for the comparison of the field- and wavelength-dependent efficiencies of a refractive lens (left in b), a diffractive optical element (DOE, blazed-grating, center in b), and a metalens (right in b). For comparison, the respective lenses are discretized in five radial sections with the corresponding deflection angles α (lattice constants, NA values) from $\alpha = 0°$ to $\alpha = 53°$. The resulting absolute deflection efficiencies are calculated. The lens is modeled as a refractive prism, while the DOE and metalens are modeled in a periodic setting with the corresponding lattice constant as given by 532 nm divided by $\sin(\alpha)$. The DOE and the metalens are positioned on a glass substrate ($n = 1.5$).

In order to shed light on the field-dependent and wavelength-dependent focusing efficiencies and to put them into a broader context, we perform numerical simulations to extract the focusing efficiencies of a refractive lens, a diffractive lens, and a metalens. We then discuss the performances for these three cases in terms of the spectral and angular bandwidth as well as their absolute lens efficiencies. For this purpose, we discretize the lenses along the radial direction in five areas corresponding to fixed deflection angles $\alpha_i = 0°$, 8°, 17°, 32°, and 53° (corresponding to $NA_i = 0$, 0.13, 0.26, 0.53, and 0.8) in order to calculate the absolute deflection efficiencies for each area with respect to field angle θ and wavelength λ (Figure 5 a). The deflection efficiency is calculated as the ratio of the transmitted power at the designed diffraction order of the respective lens with respect to the power of the incident light. For the refractive lens, we assume a refractive prism with a refractive index $n = 1.5$ and various slopes that correspond to the respective deflection angles. For the diffractive optical element (DOE) and the metalens, we perform numerical simulations of a periodic lattice of blaze profiles ($n = 1.5$) and metalens unit cells, respectively, with the lattice constants of the supercells resulting in the desired diffraction angles of the first order. The center-to-center distance of the PIM pillars is fixed to 250 nm. Figure 5b shows schematic diagrams of the sawtooth and nanopillar design for the unit cell. The plots for the simulated deflection efficiencies are shown in Figure 6 for the three cases. Note that the plots are inherently asymmetric with respect to field angle. The refractive lens case serves as a benchmark for the remaining two cases since its overall performance is superior compared to the other two cases.

In terms of operation wavelength, the metalens shows the smallest spectral bandwidth which also explains the stopping down of the PIM's numerical aperture for 405 and 660 nm wavelength as observed before. The blazed grating performs much better in this respect; however, for larger deflection angles (smaller lattice constants) the efficiencies quickly deteriorate due to interferences and shadowing effects of the blaze profile—especially for high deflection and field angles. Also, the occurrence of Rayleigh anomalies results in pronounced dips in the efficiency curves and is clearly visible in Figure 6f–h. The resulting reduction of angular bandwidth ultimately results in a field-dependent reduction of resolution and vignetting of the image.

As opposed to the DOE, the metalens' angular bandwidth is much larger, and therefore, the aforementioned effects are reduced. This leads us to the conclusion that the metalens is superior to the DOE with respect to the angular bandwidth due to its flat configuration. This is particularly important since the angular bandwidth is directly related to the etendue of the lens and, therefore, an important measure of how much light can be transported within an imaging optical system. In order to quantify the spectral and angular bandwidth we draw the contour line with a deflection efficiency of $\eta = 0.6$ (black lines in Figure 6) and read out the minimum spectral and angular bandwidth for the three cases. In our case, the obtained angular bandwidth is $\Delta\theta < 40°$ for the lens and the metalens and $\Delta\theta < 10°$ for the DOE. The respective spectral bandwidths are $\Delta\lambda >$ 250 nm (lens), $\Delta\lambda >$ 230 nm (DOE), and $\Delta\lambda <$ 140 nm (PIM). Notably, we use standard materials for the respective devices. For high-refractive index materials, a general decrease of structure height is expected that can improve the angular

DOI: 10.1021/acsphotonics.9b00221
ACS Photonics 2019, 6, 1493−1499

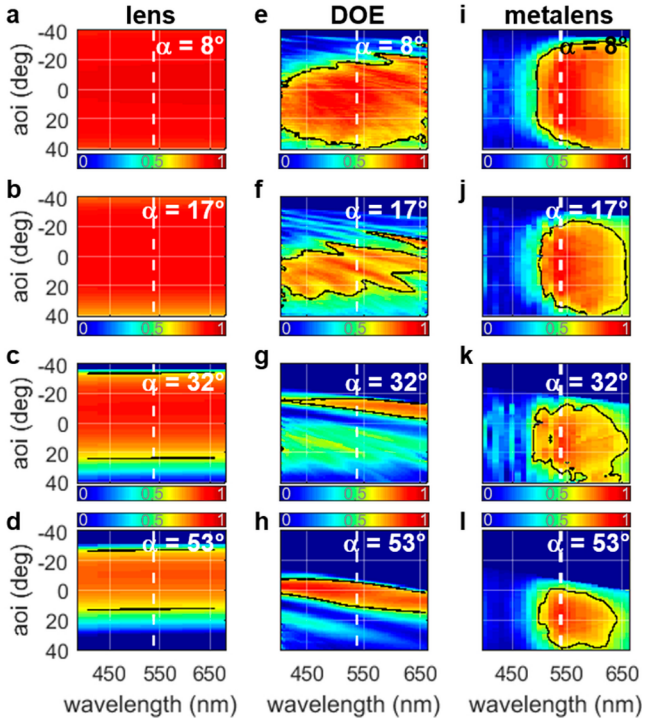

Figure 6. (a) Simulated absolute deflection efficiencies (normalized to the incident power, the color scale is from 0/blue to 1/red for all images) at λ = 400−660 nm wavelengths and for θ = −40° to θ = +40° incidence angles for the refractive lens, the DOE, and the metalens (columns). Each row represents the results for a fixed deflection angle of α = 8° (a, e, i), 17° (b, f, j), 32° (c, g, k), and 53° (d, h, l) that corresponds to one section of the discretized lens, as shown in Figure 5. The white-dashed line marks the efficiency data that is used in Figure 7.

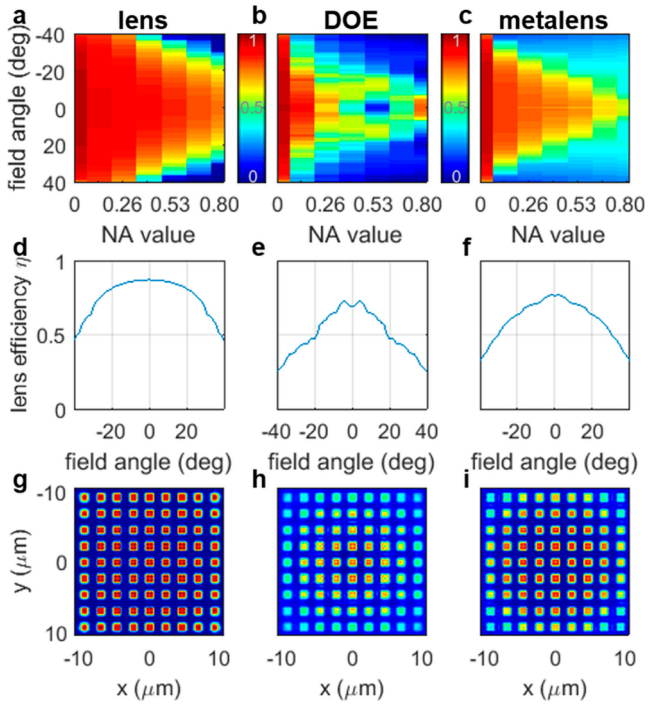

Figure 7. (a−c) Simulated deflection efficiencies (color scale is from 0/blue to 1/red for all images) for λ = 532 nm wavelength for the refractive lens, the DOE, and the metalens (columns). (d−f) Total deflected efficiency η of the entire lenses depending on field angle θ. (g−i) Imaging simulation of an array of square patches sized three times the diffraction-limited spot size (sampling is 2× Nyquist). The color scale is from 0 intensity (blue) to maximum intensity (red) for ideal imaging.

behavior of the DOE; however, the increased dispersion that is usually connected to high-index materials also decreases spectral bandwidth.

In a final step, we assess the metalens performance in comparison with a refractive lens and a DOE. Since singlet lenses, unlike multilens objectives, generally suffer from severe coma we use a simplified image simulation to connect the field-dependent lens efficiencies with the imaging properties in terms of image uniformity, vignetting, and image resolution. In this way, our comparison is not dominated by coma and the effects of efficiency variations become obvious. Our image simulation under monochromatic illumination (λ = 532 nm) utilizes the field- and position-dependent (radial distance from the center of the lens) efficiencies $\eta(\theta,\alpha)$ as amplitude function in the pupil of the lens, as shown in Figure 7a−c. These results were obtained by an additional processing of the simulation data shown in Figure 6. For clarity, no geometrical wavefront aberrations (spherical aberrations, coma, astigmatism, etc.) were taken into account. We also calculate the total lens efficiency (Figure 7d−f) as a function of field angle in order to estimate the vignetting caused by the efficiency drop for larger angles of incidence. Again, the refractive lens will serve as a benchmark for the DOE and the PIM performance.

We find that, as compared to the DOE, the PIM efficiencies are more homogeneous over the lens radius (NA value) and the angular bandwidth is higher than for the DOE (Figure 7b,c). This results in a higher total lens efficiency (Figure 7e,f) for off-axis objects and leads to a better resolution for off-axis squares. Notably, for a lens coordinate corresponding to an NA value around 0.5, the DOE's on-axis efficiency shows a pronounced minimum (see Figure 7b) that also translates to a dip in total lens efficiency at a field angle of θ = 0° (see Figure 7e). Generally, the overall lens efficiency, as shown in Figure 7d−f, is decreasing for higher field angles and will manifest itself as vignetting in the image.

In order to obtain a better understanding of how the efficiency characteristics contribute to the image formation, we now multiply the object spectrum of an array of square patches with the calculated pupil function and calculate the image via Fourier transformation.

This also allows us to visualize the 2D resolution variations of the lens for imaging purposes that are not captured by an MTF representation. For the imaging object, we choose an array of squares with a lattice constant of approximately 2 μm and a square size of 1 μm (the diffraction-limited spot size of the NA = 0.8 system at 532 nm wavelength is approximately 330 nm). To gain useful insights into the ramifications of the efficiency behavior on the imaging performance, we compensate for the coma that would otherwise be dominant for singlet lenses. The calculated images are shown in Figure 7g−i. The pixel size of the object is chosen so that the sampling of the image is 2× Nyquist sampling and the size of the patches is 7 × 7 pixels to visualize the effects of the lens efficiencies on the resolution. The most obvious aspect of the image simulation is the aforementioned vignetting of the images especially for the DOE and the PIM, with the vignetting being stronger for the DOE. Upon closer analysis, one can also observe the decrease in resolution for larger field

DOI: 10.1021/acsphotonics.9b00221
ACS Photonics 2019, 6, 1493−1499

angles that is connected to the maximum lens efficiency and is dependent on the deflection angle (NA value). Since this efficiency is higher for the PIM (Figure 7c), the resolution of the PIM is better than for the DOE. Also, the pronounced efficiency drops for an NA value of 0.5 at $\theta = 0°$ for the DOE (Figure 7b) can be identified in the image simulation and results in an edge enhancement at the central patches resembling high pass filtering. This effect is not observed for the refractive lens and for the PIM.

It is worth mentioning that the PIM design relies on its constituent nanostructures, which contains numerous degrees of freedom to improve efficiency. If one can consider engineering the dispersion of each constituent nanostructure, it is possible to increase its spectral[23−29] and angular[36−40] bandwidth. The constituent nanostructures can even possess freeform, irregular shapes using methods such as topology optimization. Recently, it has been shown that, by inverse design methods, that metasurfaces can reach an efficiency of 95% also for large deflection angles.[41]

SUMMARY AND CONCLUSIONS

In summary, we have shown a comprehensive and rigorous aberration analysis of a polarization-independent metalens depending on field angle and wavelength. We have experimentally retrieved the wavefront aberrations via a phase-retrieval algorithm and identified the main aberrations dependent on angle of incidence and wavelength. While for on-axis illumination at the design wavelength the PIM performance is diffraction-limited, we found that, for off-axis illumination, the coma originating from the violation of the Abbe sine condition is the limiting aberration. The other Zernike coefficients stay reasonably low even for larger field angles. We also observed a reduction of the effective numerical aperture of the PIM from NA = 0.8 to NA = 0.5 for operation wavelengths away from the design wavelength. At these wavelengths, the dominating wavefront aberrations are spherical aberrations that show weak dependence on field angle. This implies that the PIM can perform satisfactory imaging away from its design wavelength.

In a final step, we have investigated the imaging performance of our PIM in comparison with refractive and diffractive lenses. For this purpose, we have performed an image simulation for these three cases based on the field-dependent and wavelength-dependent absolute deflection efficiencies gained from numerical simulations. We find that, while refractive lenses naturally perform best, our PIM outperforms the diffractive lens with respect to angular bandwidth (leading to a better etendue) and total lens efficiency. However, the spectral bandwidth of the PIM is smaller than for the diffractive lens, which can be further improved by dispersion engineering or topology optimization. Our image simulation also shows that the diffractive lens suffers from pronounced efficiency variations with angles of incidence leading to field-dependent resolution variations and vignetting. These effects are absent for the PIM, which shows a smooth decrease of efficiency for larger field angles, similar to refractive lenses.

In conclusion, metalenses are in principle well suited for imaging systems if field-dependent aberrations and field-dependent efficiency variations can be reduced or even eliminated. Ideally, also strategies for the mitigation of the strong dispersion of the metalens' elements need to be found to allow for high quality broadband imaging of extended objects. While solution strategies for each of these challenges exist, the combination of all strategies proves to be difficult. Nevertheless, the degrees of freedom offered by tailoring the design of the underlying nanostructures in the metalens have the potential to address these challenges.

AUTHOR INFORMATION

Corresponding Author

*E-mail: manuel.decker@zeiss.com.

ORCID

Manuel Decker: 0000-0002-9125-0851

Wei Ting Chen: 0000-0001-8665-9241

Notes

The authors declare no competing financial interest.

ACKNOWLEDGMENTS

This work was supported by the Air Force Office of Scientific Research (MURI, Grant Nos. FA9550-14-1-0389 and FA9550-16-1-0156) and the Defense Advanced Research Projects Agency (Grant No. HR00111810001). This work was performed in part at the Center for Nanoscale Systems (CNS), a member of the National Nanotechnology Coordinated Infrastructure Network (NNCI), which is supported by the National Science Foundation under NSF Award No. 1541959.

REFERENCES

(1) Arbabi, A.; Horie, Y.; Bagheri, M.; Faraon, A. Dielectric metasurfaces for complete control of phase and polarization with subwavelength spatial resolution and high transmission. *Nat. Nanotechnol.* **2015**, *10*, 937−943.

(2) Genevet, P.; Capasso, F.; Aieta, F.; Khorasaninejad, M.; Devlin, R. Recent advances in planar optics: from plasmonic to dielectric metasurfaces. *Optica* **2017**, *4*, 139−152.

(3) Bomzon, Z. E.; Kleiner, V.; Hasman, E. Pancharatnam-Berry phase in space-variant polarization-state manipulations with subwavelength gratings. *Opt. Lett.* **2001**, *26*, 1424−1426.

(4) Lalanne, P.; Chavel, P. Metalenses at visible wavelengths: past, present, perspectives. *Laser Photon. Rev.* **2017**, *11*, 1600295.

(5) Arbabi, A.; Horie, Y.; Ball, A. J.; Bagheri, M.; Faraon, A. Subwavelength-thick lenses with high numerical apertures and large efficiency based on high-contrast transmitarrays. *Nat. Commun.* **2015**, *6*, 7069.

(6) Lin, D.; Fan, P.; Hasman, E.; Brongersma, M. L. Dielectric gradient metasurface optical elements. *Science* **2014**, *345*, 298−302.

(7) Khorasaninejad, M.; Chen, W. T.; Devlin, R. C.; Oh, J.; Zhu, A. Y.; Capasso, F. Metalenses at visible wavelengths: Diffraction-limited focusing and subwavelength resolution imaging. *Science* **2016**, *352*, 1190−1194.

(8) Khorasaninejad, M.; Capasso, F. Metalenses: Versatile multifunctional photonic components. *Science* **2017**, *358*, 8100.

(9) She, A.; Zhang, S.; Shian, S.; Clarke, D. R.; Capasso, F. Large area metalenses: design, characterization, and mass manufacturing. *Opt. Express* **2018**, *26*, 1573−1585.

(10) Lee, M. S. L.; Lalanne, P.; Rodier, J. C.; Chavel, P.; Cambril, E.; Chen, Y. Imaging with blazed-binary diffractive elements. *J. Opt. A: Pure Appl. Opt.* **2002**, *4*, S119.

(11) Decker, M.; Staude, I.; Falkner, M.; Dominguez, J.; Neshev, D. N.; Brener, I.; Pertsch, T.; Kivshar, Y. S. High-efficiency dielectric Huygens' surfaces. *Adv. Opt. Mater.* **2015**, *3*, 813−820.

(12) Chong, K. E.; Staude, I.; James, A.; Dominguez, J.; Liu, S.; Campione, S.; Subramania, G. S.; Luk, T. S.; Decker, M.; Neshev, D. N.; Brener, I.; Kivshar, Y. S. Polarization-independent silicon metadevices for efficient optical wavefront control. *Nano Lett.* **2015**, *15* (2015), 5369−5374.

DOI: 10.1021/acsphotonics.9b00221
ACS Photonics 2019, 6, 1493−1499

(13) Chong, K. E.; Wang, L.; Staude, I.; James, A. R.; Dominguez, J.; Liu, S.; Subramania, G. S.; Decker, M.; Neshev, D. N.; Brener, I.; Kivshar, Y. S. Efficient polarization-insensitive complex wavefront control using Huygens' metasurfaces based on dielectric resonant meta-atoms. *ACS Photonics* **2016**, *3*, 514−519.
(14) Kuznetsov, A. I.; Miroshnichenko, A. E.; Brongersma, M. L.; Kivshar, Y. S.; Luk'yanchuk, B. Optically resonant dielectric nanostructures. *Science* **2016**, *354*, 2472.
(15) Decker, M.; Staude, I. Resonant dielectric nanostructures: a low-loss platform for functional nanophotonics. *J. Opt.* **2016**, *18*, 103001.
(16) Chen, B. H.; Wu, P. C.; Su, V.-C.; Lai, Y.-C.; Chu, C. H.; Lee, I. C.; Chen, J.-W.; Chen, Y. H.; Lan, Y.-C.; Kuan, C.-H.; Tsai, D. P. GaN Metalens for Pixel-Level Full-Color Routing at Visible Light. *Nano Lett.* **2017**, *17*, 6345.
(17) Colburn, S.; Zhan, A.; Majumdar, A. Metasurface optics for full-color computational imaging. *Sci. Adv.* **2018**, *4*, 2114.
(18) Paniagua-Dominguez, R.; Yu, Y. F.; Khaidarov, E.; Choi, S.; Leong, V.; Bakker, R. M.; Liang, X.; Fu, Y. H.; Valuckas, V.; Krivitsky, L. A.; Kuznetsov, A. I. A metalens with a near-unity numerical aperture,. *Nano Lett.* **2018**, *18*, 2124−2132.
(19) Chen, W. T.; Zhu, A. Y.; Khorasaninejad, M.; Shi, Z.; Sanjeev, V.; Capasso, F. Immersion Meta-Lenses at Visible Wavelengths for Nanoscale Imaging. *Nano Lett.* **2017**, *17*, 3188−3194.
(20) Liang, H.; Lin, Q.; Xie, X.; Sun, Q.; Wang, Y.; Zhou, L.; Liu, L.; Yu, X.; Zhou, J.; Krauss, T. F.; Li, J. An Ultra-high Numerical Aperture Metalens at Visible Wavelengths. *Nano Lett.* **2018**, *18*, 4460−4466.
(21) Byrnes, S. J.; Lenef, A.; Aieta, F.; Capasso, F. Designing large, high-efficiency, high-numerical-aperture, transmissive meta-lenses for visible light. *Opt. Express* **2016**, *24*, 5110−5124.
(22) Khorasaninejad, M.; Zhu, A. Y.; Roques-Carmes, C.; Chen, W. T.; Oh, J.; Mishra, I.; Devlin, R. C.; Capasso, F. Polarization-insensitive metalenses at visible wavelengths. *Nano Lett.* **2016**, *16*, 7229−7234.
(23) Chen, W. T.; Zhu, A. Y.; Sanjeev, V.; Khorasaninejad, M.; Shi, Z.; Lee, E.; Capasso, F. A broadband achromatic metalens for focusing and imaging in the visible. *Nat. Nanotechnol.* **2018**, *13*, 220−226.
(24) Wang, S.; Wu, P. C.; Su, V.-C.; Lai, Y.-C.; Chen, M.-K.; Kuo, H. Y.; Chen, B. H.; Chen, Y. H.; Huang, T.-T.; Wang, J.-H.; Lin, R.-M.; Kuan, C.-H.; Li, T.; Wang, Z.; Zhu, S.; Tsai, D. P. A broadband achromatic metalens in the visible. *Nat. Nanotechnol.* **2018**, *13*, 227−232.
(25) Li, Y.; Li, X.; Pu, M.; Zhao, Z.; Ma, X.; Wang, Y.; Luo, X. Achromatic flat optical components via compensation between structure and material dispersions. *Sci. Rep.* **2016**, *6*, 19885.
(26) Avayu, O.; Almeida, E.; Prior, Y.; Ellenbogen, T. Composite functional metasurfaces for multispectral achromatic optics. *Nat. Commun.* **2017**, *8*, 14992.
(27) Arbabi, E.; Arbabi, A.; Kamali, S. M.; Horie, Y.; Faraon, A. Controlling the sign of chromatic dispersion in diffractive optics with dielectric metasurfaces. *Optica* **2017**, *4*, 625−632.
(28) Hu, J.; Liu, C.-H.; Ren, X.; Lauhon, L. J.; Odom, T. W. Plasmonic lattice lenses for multiwavelength achromatic focusing. *ACS Nano* **2016**, *10*, 10275−10282.
(29) Chen, W. T.; Zhu, A. Y.; Sisler, J.; Huang, Y.-W.; Yousef, K. M. A.; Lee, E.; Qiu, C.-W.; Capasso, F. Broadband Achromatic Metasurface-Refractive Optics. *Nano Lett.* **2018**, *18*, 7801−7808.
(30) Tong, L.; Lou, J.; Mazur, E. Single-mode guiding properties of subwavelength-diameter silica and silicon wire waveguides. *Opt. Express* **2004**, *12*, 1025−1035.
(31) Fienup, J. R. Phase-retrieval algorithms for a complicated optical system. *Appl. Opt.* **1993**, *32*, 1737−46.
(32) Gross, H. *Handbook of Optical Systems*; Wiley-VCH: Weinheim, Berlin, Germany, 2005; Vol. *1*.
(33) Geary, J. M. *Introduction to Lens Design: With Practical ZEMAX Examples*; Willmann-Bell: Richmond, VA, 2002.
(34) Groever, B.; Chen, W. T.; Capasso, F. Meta-Lens Doublet in the Visible Region. *Nano Lett.* **2017**, *17*, 4902−4907.
(35) Arbabi, A.; Arbabi, E.; Kamali, S. M.; Horie, Y.; Han, S.; Faraon, A. Miniature optical planar camera based on a wide-angle metasurface doublet corrected for monochromatic aberrations. *Nat. Commun.* **2016**, *7*, 13682.
(36) Lin, Z.; Groever, B.; Capasso, F.; Rodriguez, A. W.; Lončar, M. Topology-Optimized Multilayered Metaoptics. *Phys. Rev. Appl.* **2018**, *9*, 044030.
(37) Kamali, S. M.; Arbabi, E.; Arbabi, A.; Horie, Y.; Faraji-Dana, M.; Faraon, A. Angle-Multiplexed Metasurfaces: Encoding Independent Wavefronts in a Single Metasurface under Different Illumination Angles. *Phys. Rev. X* **2017**, *7*, 041056.
(38) Liu, W.; Li, Z.; Cheng, H.; Tang, C.; Li, J.; Zhang, S.; Chen, S.; Tian, J. Metasurface Enabled Wide-Angle Fourier Lens. *Adv. Mater.* **2018**, *30*, 1706368.
(39) Akbarzadeh, A.; Chamanara, N.; Caloz, C. Inverse prism based on temporal discontinuity and spatial dispersion. *Opt. Lett.* **2018**, *43*, 3297−3300.
(40) Qiu, M.; Jia, M.; Ma, S.; Sun, S.; He, Q.; Zhou, L. Angular Dispersions in Terahertz Metasurfaces: Physics and Applications. *Phys. Rev. Appl.* **2018**, *9*, 054050.
(41) Sell, D.; Yang, J.; Doshay, S.; Yang, R.; Fan, J. A. Large-Angle, Multifunctional Metagratings Based on Freeform Multimode Geometries. *Nano Lett.* **2017**, *17*, 3752−3757.

DOI: 10.1021/acsphotonics.9b00221
ACS Photonics 2019, 6, 1493−1499